10-1-2015

Quantifying Cross-scatter Contamination in Biplane Fluoroscopy Motion Analysis Systems

Janelle A. Cross
Marquette University, janelle.cross@marquette.edu

Ben McHenry
Marquette University, ben.mchenry@marquette.edu

Taly Gilat-Schmidt
Marquette University, tal.gilat-schmidt@marquette.edu

Published version. *Journal of Medical Imaging*, Vol. 2, No. 4 (Oct.-Dec. 2015). DOI.

Quantifying cross-scatter contamination in biplane fluoroscopy motion analysis systems

Janelle A. Cross, Ben McHenry, and Taly Gilat Schmidt*
Marquette University, Department of Biomedical Engineering, 1515 W. Wisconsin Avenue, Milwaukee, Wisconsin 53233, United States

Abstract. Biplane fluoroscopy is used for dynamic *in vivo* three-dimensional motion analysis of various joints of the body. Cross-scatter between the two fluoroscopy systems may limit tracking accuracy. This study measured the magnitude and effects of cross-scatter in biplane fluoroscopic images. Four cylindrical phantoms of 4-, 6-, 8-, and 10-in. diameter were imaged at varying kVp levels to determine the cross-scatter fraction and contrast-to-noise ratio (CNR). Monte Carlo simulations quantified the effect of the gantry angle on the cross-scatter fraction. A cadaver foot with implanted beads was also imaged. The effect of cross-scatter on marker-based tracking accuracy was investigated. Results demonstrated that the cross-scatter fraction varied from 0.15 for the 4-in. cylinder to 0.89 for the 10-in. cylinder when averaged across kVp. The average change in CNR due to cross-scatter ranged from 5% to 36% CNR decreases for the 4- and 10-in. cylinders, respectively. In simulations, the cross-scatter fraction increased with the gantry angle for the 8- and 10-in. cylinders. Cross-scatter significantly increased static-tracking error by 15%, 25%, and 38% for the 6-, 8-, and 10-in. phantoms, respectively, with no significant effect for the foot specimen. The results demonstrated submillimeter marker-based tracking for a range of phantom sizes, despite cross-scatter degradation. [DOI: 10.1117/1.JMI.2.4.043503]

Keywords: biplane fluoroscopy; cross-scatter; scatter fraction; contrast-to-noise ratio; marker-based tracking.

Paper 15087RR received Apr. 17, 2015; accepted for publication Sep. 24, 2015; published online Oct. 23, 2015.

1 Introduction

Biplane fluoroscopy is an emerging technology for three-dimensional (3-D) motion analysis that has been used to analyze dynamic *in vivo* motion of the bones in the shoulder,[1] spine,[2,3] and knee.[4,5] The ability to directly analyze joints within the body to attain reliable *in vivo* kinematics is beneficial for biomechanical research and will potentially impact surgical and orthoses modifications in orthopedic disorders. Conventional methods of motion analysis that track skin-mounted optical markers with motion cameras have been shown to introduce skin movement artifacts due to relative movement between the markers and underlying bones.[6,7] For example, in a foot/ankle study, the two malleoli markers showed the largest artifact with the mean displacement between skin markers and bones varying from 2.7 to 14.9 mm.[8] Fluoroscopy is a noninvasive method that can directly capture *in vivo* skeletal motion, which not only circumvents skin movement artifacts but also allows for motion tracking of joints that are either too subcutaneous for conventional methods (such as the spine) or are obscured by a rehabilitative device (such as the shod foot/ankle).

In marker-based fluoroscopic motion tracking, implanted tantalum beads are used to track individual bones. A minimum of three beads per bone segment is required for 3-D analysis.[9] This is an invasive procedure that is limited to subjects who are undergoing a surgical procedure at the same time as implantation.[1] Markerless or model-based fluoroscopic methods may be used to avoid the invasiveness of implanted beads.[10] Model-based methods determine the bone positions and orientations by comparing a 3-D bone model from a computed tomography (CT) or magnetic resonance imaging (MRI) scan to the acquired biplane fluoroscopic images. Marker-based studies are typically used as the "gold standard" when evaluating the accuracy of and validating model-based tracking methods and software.

As in conventional x-ray imaging, the detected image is degraded by photons scattered from the primary beam. In biplane fluoroscopy, additional scattered photons are detected that originated from the second x-ray source, which is referred to as cross-scatter. Cross-scatter is a potential source of degradation in biplane fluoroscopy motion analysis, as the two biplane images are typically synchronously acquired to enable accurate localization of the bone segments at each time point. Previous studies of dual-source CT imaging found cross-scatter to be a considerable source of degradation, in some cases a larger component than the forward scatter signal.[11–13] In CT imaging, cross-scatter increased artifacts and reduced the contrast-to-noise ratio (CNR).[12,13] The spatial distribution of the cross-scatter signal was found to be asymmetrical and dependent on the size and shape of the imaged object.[11–13]

The purpose of this study was to quantify the magnitude and effects of cross-scatter in fluoroscopic images acquired with a biplane x-ray imaging system over a range of object sizes, kVp settings, and gantry angles. This study also quantified the effects of cross-scatter on the accuracy of marker-based tracking. Quantifying the effects of cross-scatter on motion tracking is important for determining whether scatter rejection methods should be developed for this specific application of high-speed motion tracking.

*Address all correspondence to: Taly Gilat Schmidt, E-mail: tal.gilat-schmidt@marquette.edu

2329-4302/2015/$25.00 © 2015 SPIE

2 Methodology

2.1 *Hardware*

A biplane fluoroscopy system for motion and kinetic analysis of the bare and shod foot was constructed with a fixed gantry angle of 60 deg (Fig. 1). The system was centered along a raised walkway with an embedded 46.4 × 50.8 cm force plate (AMTI OR6-500 6-DOF, Watertown, Massachusetts). Two x-ray sources (OEC 9000, GE Healthcare, Chalfont St. Giles) and two 15-in. image intensifiers (Dunlee, Aurora, Illinois) were mounted to the walkway with a 60-deg angle between the sources. High-speed cameras (N4, IDT, Pasadena, California) with 52 mm lenses (Nikon, Melville, New York) were attached to each image intensifier (II). The images were captured and digitized directly to a controller PC via Motion Studio 64 (Version 2.10.05, IDT, Pasadena, California). The source-to-detector and source-to-object-center distances were 112 cm and 76 cm, respectively, for both source–intensifier pairs.

2.2 *Phantoms and X-Ray Settings*

Four cylindrical water phantoms of height 12 in. and of diameters 4, 6, 8, and 10 in. were imaged. The 4-in. cylinder represented the ankle, the 6-in. cylinder the knee, the 8-in. cylinder the shoulder, and the 10-in. cylinder the spine or hip. A 1-in. diameter Teflon sphere was suspended in the center of the phantoms for measuring contrast. Teflon was chosen because it provides a high-contrast feature similar to bone. Conspicuity of the bone features is important for model-based motion tracking methods.[14] For each phantom, images were acquired at kVp settings of 60, 70, 80, 90, 100, and 110 kVp with mA settings of 5.0, 5.0, 4.5, 3.5, 2.5, and 2.2 mA, respectively. The inherent beam filtration was equivalent to 2.5 mm of aluminum per manufacturer specifications. The tube current values were varied in order to provide similar detected image intensities (±5%) across the kVp level at the center of the 6-in. diameter cylinder, which represented a medium object size. An in-beam chamber (RadCal 10x6-6, Monrovia, California) was placed at the center of the field of view (FOV) where the central rays of the gantries crossed. The fluoroscopy units were turned on for 2 s, the approximate length of one gait trial, and the exposure was measured at the selected kVp and mA levels (Table 1). Experiments also verified that the detected signal was linear with exposure over the range of kVp and mA settings used in this study.

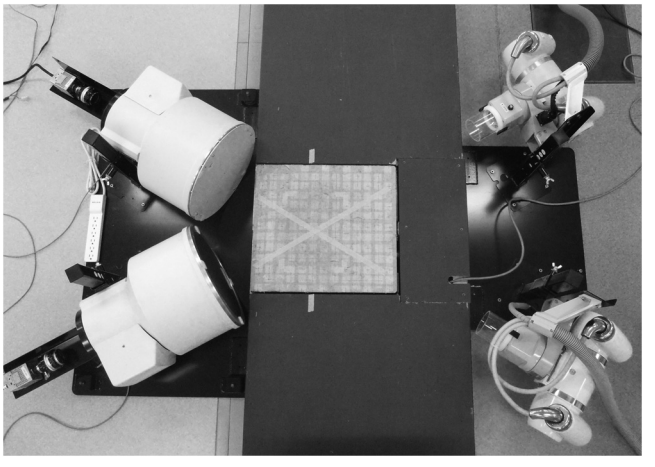

Fig. 1 Custom-built biplane fluoroscopy system with x-ray sources attached to right-hand side of walkway and image intensifiers attached to left-hand side. The embedded force plate is placed where the x-ray beams intersect.

Table 1 Exposure measurements of biplane system for 2 s of exposure.

kVp	mA	*R*
60	5.0	0.115
70	5.0	0.157
80	4.5	0.190
90	3.5	0.199
100	2.5	0.191
110	2.2	0.214

Images containing primary, scatter, and cross-scatter signals (primary+scatter+cross_scatter) were collected by imaging with both sources on. In this work, we use "primary+scatter" to refer to the signal detected by one II from the beam that is focused on that II. We use "cross-scatter" to refer to the signal detected by one II from the beam that is focused on the second II. Images were then acquired with one source turned off, such that one II collected images without cross-scatter (primary+scatter), while the second II collected images of only cross-scatter and no primary signal. Fifty images were acquired (sampling frequency of 200 Hz) for each phantom, kVp setting, and scatter condition.

2.3 *Cadaver Specimen and Computed Tomography*

To provide a realistic simulation of the *in vivo* condition, a fresh-frozen trans-tibial cadaver foot from a 34-year-old male was obtained subject to institutional review board approval. Three 1.6-mm diameter steel beads were implanted into each of the three hindfoot bones (calcaneus, talus, and tibia) with minimal dissection of the surrounding soft tissues by an orthopedic surgeon. A 2-mm hole was drilled into the cortical bone so that the beads could be manually pressed into the hole until flush with the bone. The beads were then secured into place using cyanoacrylate adhesive.

A CT scan of the cadaver foot was obtained consisting of 956 transverse-plane slices, each 0.625mm thick (512 × 512 pixels; LightSpeed VCT, GE Healthcare, Milwaukee, Wisconsin), to obtain the locations of the beads. An image processing algorithm was implemented in MATLAB® (MathWorks, Natick, Massachusetts) to determine the subpixel bead centroids, which represented the gold-standard bead locations.

To simulate joints with more soft tissue, the foot specimen was also imaged with water-filled boxes of thickness 1.5 and 3 in. placed on the source side of the foot. Static images of the foot were collected at the same tube voltage and current as the water phantoms.

2.4 *Scatter Fraction and Contrast-to-Noise Ratio*

Regions of interest (ROIs) of size 30 × 30 pixels were extracted from the water background (ROI1) and Teflon sphere (ROI2) in all the collected images of the water cylinders. The background

ROI was located at the center of the FOV. The Teflon ROI was laterally located at the center of the FOV with height 1 in. above the FOV center. For the cadaver foot specimen, cross-scatter was quantified in a 30×30 pixel ROI extracted from a uniform region at the center of the FOV. These ROIs were used to calculate the cross-scatter fraction (CSF) and the percentage change in the CNR due to cross-scatter. The CSF was calculated in the centered, background ROI as

$$\mathrm{CSF} = \frac{\overline{ROI1}_{\mathrm{cross\,scatter}}}{\overline{ROI1}_{\mathrm{primary+scatter}}}. \quad (1)$$

The CNR was calculated for the Teflon bead in images acquired with and without cross-scatter as

$$\mathrm{CNR} = \frac{|\overline{\mathrm{ROI1}} - \overline{\mathrm{ROI2}}|}{\sigma_{\mathrm{ROI1}}}. \quad (2)$$

The percentage change in CNR due to cross-scatter was calculated at the center of the FOV as

$$\%\mathrm{CNR} = 100 * \left(1 - \frac{\mathrm{CNR}_{\mathrm{primary+scatter+cross\,scatter}}}{\mathrm{CNR}_{\mathrm{primary+scatter}}}\right). \quad (3)$$

2.5 *Effects of Gantry Angle on Cross-Scatter*

The gantry angle is the angle between the central ray of the two fluoroscopes. The system used in this study (Fig. 1) has a fixed gantry angle of 60 deg. Previous biplane fluoroscopy motion analysis studies have reported gantry angles ranging from 45 deg to 90 deg.[1,2,4] The amount of detected cross-scatter is expected to vary with gantry angle. The effects of gantry angle could not be experimentally quantified in this study due to the fixed system geometry (Fig. 1). Therefore, Monte Carlo simulations were performed to quantify cross-scatter fraction across a range of gantry angles.

The biplane fluoroscopy system was modeled using the GEANT4 software.[15] The simulations modeled Compton scatter, Rayleigh scatter, and photoelectric absorption and tracked 10^9 photons for each simulated case. The simulations included multiple scatter, as all photons and secondary particles were tracked until they either reached the detector or exited the geometry boundary, or until their energy was below the value needed to travel 1 mm, in which case the particles were locally absorbed. X-ray spectra were modeled at 60, 80, and 100 kVp and 2.5-mm aluminum filtration using the SPEC78 software.[16] As in the experimental system, the source-to-detector distance (SDD) was 112 cm, the source-to-object-center distance (SOD) was 76 cm, and the simulated beam was collimated to illuminate the 15-in. diameter face of the IIs. The simulations modeled an ideal 15×15 in. detector, resulting in images of the primary and scattered signals across the entire detector. Simulations were performed with gantry angles of 60 deg, 75 deg, and 90 deg for each of the four cylindrical water phantoms. Gantry angles less than 60 deg could not be simulated using these specific SOD and SDD configurations due to overlap of the detectors. Simulations were performed with and without the force plate, which was modeled as an $18 \times 18 \times 1.5$ in. plate of aluminum.

The CSF was calculated for each gantry angle, phantom, and kVp setting, using ROIs at the center of the detected images, as in the experimental study. To validate the simulation methods, the CSFs estimated from the simulations at 60 deg were compared to the experimental measurements.

2.6 *Effects of Cross-Scatter on Marker-Based Tracking Accuracy*

To determine the effects of cross-scatter contamination on the accuracy of marker-based tracking, a rectangular acrylic plate (50 mm long, 16 mm wide, and 2.3 mm thick) with two 2-mm steel beads separated by 30 mm (± 0.03) was suspended in the center of the water phantoms. The water phantoms were then placed on the walkway at the intersection of the two beams. Static images were collected with both x-ray sources on to obtain primary+scatter+cross_scatter images. Images were collected with one source on and the other off to obtain image sequences containing the primary+scatter signal for one II. The on/off status of each source was reversed to acquire primary +scatter signal for the second II. A similar procedure was performed for the cadaver foot specimen with and without the added water background. For marker tracking in both the water cylinders and foot specimen, images were collected with the x-ray sources set at 90 kVp and 3.5 mA. Due to the unrepeatable motion of the acrylic plate through the water, the effects of cross-scatter were only quantified for static images.

The open-source-software x-ray reconstruction of moving morphology (XROMM, Brown University, Providence, Rhode Island) corrected the image intensifier distortion in the static images, after calibration using frames of 1.20-mm thick perforated steel with 3.18-mm diameter holes spaced 4.76 mm apart in a staggered pattern (Part No. 9255T641, McMaster-Carr, Robinson, New Jersey).[9] The direct linear transformation (DLT) technique is commonly used in biplanar fluoroscopic systems to define the linear transformation between the 3-D object space and the two-dimensional (2-D) image planes.[17] A 64-point calibration object with precisely positioned steel beads, as described by Brainerd et al., was manufactured and imaged with the biplane system.[9] A calibration algorithm used the bead images to determine the 11 DLT coefficients, which represent the internal parameters and orientation of the cameras.[18] After the image distortion was corrected and the volume was calibrated, marker-based tracking was performed using software developed by Hedrick.[17] In each fluoroscopic image, the bead positions were found by automatically tracking the center of the bead using an extended Kalman prediction algorithm. The bead centroid can be estimated with higher accuracy than the limiting spatial resolution of the system.[19,20] The 3-D positions of the beads were then determined from the biplane DLT data. The beads were tracked in 50 images of each water phantom and cadaver specimen. The absolute tracking error for each image was calculated as the measured distance between the beads minus the true interbead distance. The mean absolute tracking error and standard deviation for each water phantom and cadaver specimen were calculated. Statistically significant differences between the static tracking error with and without cross-scatter were analyzed using a Student's t test.

3 Results

Figure 2 displays a region of the primary+scatter image and the primary+scatter+cross_scatter image of the 4- and 10-in. water phantoms, demonstrating the negligible effect of cross-scatter for the 4-in. phantom. Figure 2 also demonstrates the increased signal and reduced contrast due to cross-scatter for the 10-in. phantom. Figure 3 displays the primary+scatter and primary

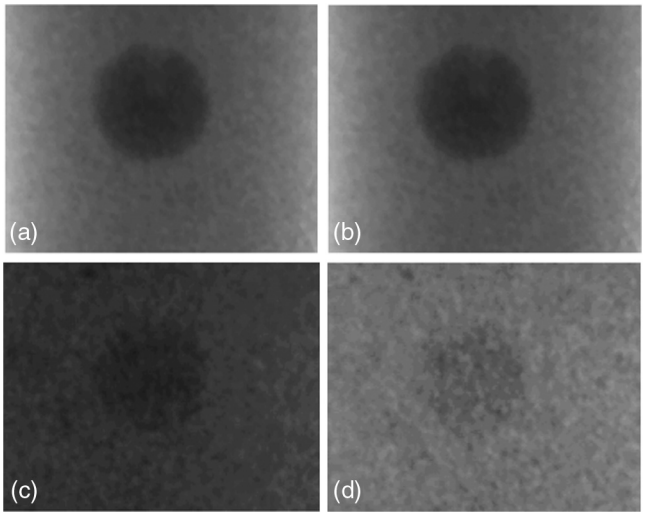

Fig. 2 X-ray images at 100 kVp of the (a) 4-in. phantom primary+scatter image and (b) 4-in. phantom primary+scatter+cross_scatter image displayed at the same window and level settings. (c) 10-in. phantom primary+scatter image, and (d) 10-in. phantom primary+scatter +cross_scatter image displayed at the same window and level settings.

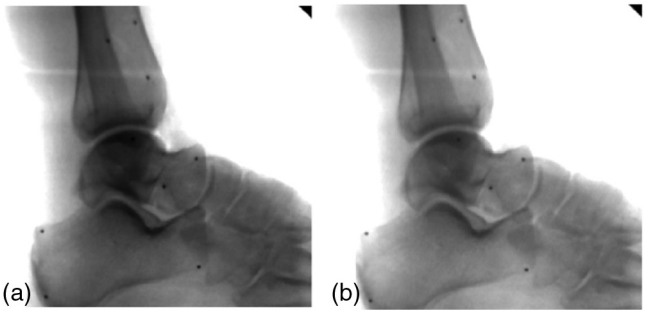

Fig. 3 X-ray images at 100 kVp of the cadaver foot specimens for the (a) primary+scatter image and (b) primary+scatter+cross_scatter image. Both images are displayed at the same window and level settings.

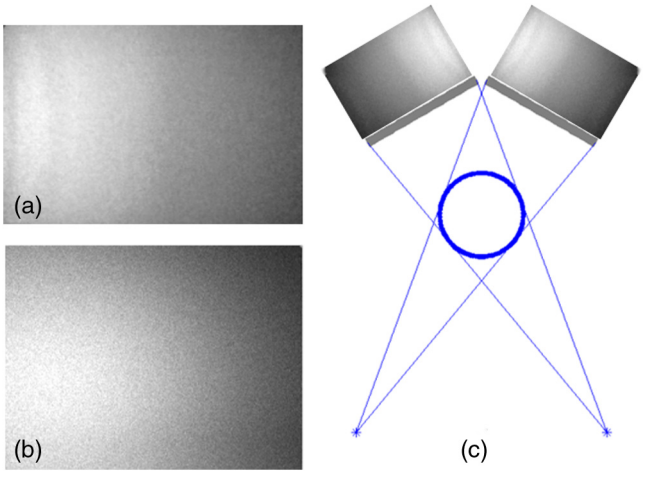

Fig. 4 (a) Experimental and (b) simulated cross-scatter image for the 10-in. diameter phantom at 100 kV and 60-deg gantry angle. Both images are windowed from zero (black) to the maximum scatter value in each image (white). (c) Orientation of the scatter images with respect to the system geometry. A quantitative comparison of the experimental and simulated cross-scatter fraction values at the center of the FOV is presented in Fig. 6.

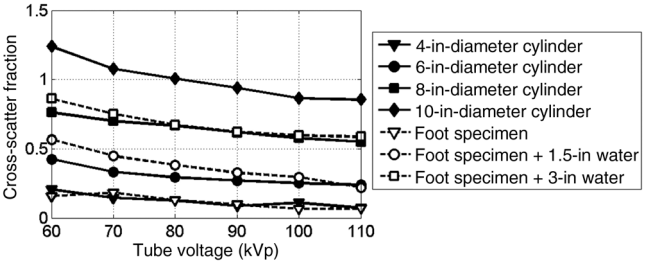

Fig. 5 Measured cross-scatter fraction for all phantoms across a range of kVp levels. Error bars, representing standard deviation, are smaller than the markers and thus are not visible.

+scatter+cross_scatter images for the foot specimen with 1.5 in. of added water background. The higher signal values in Fig. 3(b) signify the presence of cross-scatter.

Figure 4 compares the experimental and simulated cross-scatter images for the 10-in. diameter phantom and 60-deg gantry angle. The images demonstrate the asymmetrical cross-scatter distribution, with higher scatter at the edge of the detector that is closest to the cross-beam, as depicted in Fig. 4(c).

Figure 5 plots the CSF measured at the center of the FOV for a range of kVp settings for all phantom diameters. The CSF increased with phantom diameter, ranging from 0.15 for the 4-in. phantom to 0.89 for the 10-in. phantom, when averaged across kVp. The CSF decreased with increasing kVp. Cross-scatter reduced the CNR by 5% (±5%) for the 4-in. phantom, 15% (±5%) for the 6-in. phantom, 26% (±7%) for the 8-in. phantom, and 36% (±9%) for the 10-in. phantom when averaged across kVp. The percentage change in CNR did not correlate with kVp for any of the phantoms ($p > 0.1$).

Prior to quantifying the effects of gantry angle on cross-scatter, the simulation methods were validated against the experimental results at the 60-deg gantry angle. Figure 6 presents the results of the validation study, with the simulated values resulting from simulations that modeled the force plate. The experimental and simulation results demonstrated good agreement at 80 and 100 kVp (error < 10%). The 60 kVp simulations demonstrated larger discrepancies, with an average error of 13% compared to the experimental measurements. Residual error between the simulation and experimental results may be due to a variety of factors, including inaccurate modeling of the force plate and the ideal modeling of the detector response in simulation. The effects of the force place were to attenuate the cross-scatter that traveled through the force plate and to increase the cross-scatter for the remainder of the FOV. At the center of the FOV, the force plate increased cross-scatter by 25% for the 4-in. cylinder, 15% for the 6-in. cylinder, and 10% for the 8- and 10-in. cylinders. All subsequent simulation results are presented for simulations without the force plate.

Figure 7 displays the simulated scatter images for the 10-in. diameter phantom at 100 kV and scatter angles of 60 deg, 75 deg, and 90 deg, demonstrating increased scatter with gantry angle and the asymmetrical cross-scatter distribution as in the experimental images displayed in Fig. 4.

Figure 8 plots the CSF at 60 deg, 75 deg, and 90-deg gantry angles, as estimated by the Monte Carlo simulations at the center

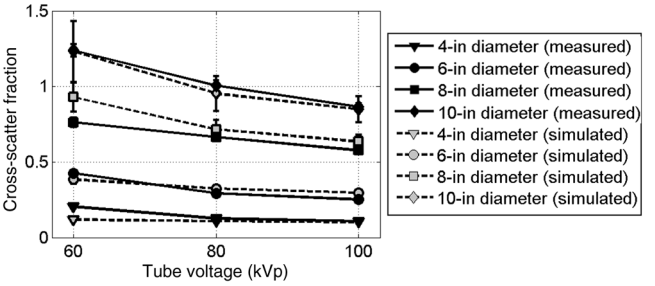

Fig. 6 Comparison of cross-scatter fraction (CSF) measured experimentally and estimated through simulations for a gantry angle of 60 deg. Error bars represent one standard deviation.

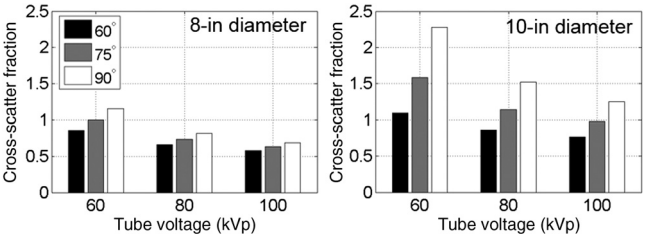

Fig. 8 Cross-scatter fractions plotted for gantry angles of 60 deg, 75 deg, and 90 deg for the 8- and 10-in. cylindrical phantoms at a range of kVp settings, as estimated through simulations. Gantry angle did not measurably affect the cross-scatter fractions for the 4- and 6-in. phantoms.

of the FOV, for the 8- and 10-in. phantoms at a range of kVp levels. The results demonstrate increased CSF with increasing gantry angle, with greater increases for the 10-in. phantom and at lower kVp settings. Gantry angle did not measurably affect the CSF for the 4- and 6-in. phantoms.

The absolute tracking error for the static trials is compared in Fig. 9 for images with and without cross-scatter. The absolute error in Fig. 9 depends on the tube current setting, which was not optimized for each object. In this study, we focused on the change in tracking error due to cross-scatter. As seen in Fig. 9, images acquired with cross-scatter demonstrated significantly increased tracking error ($p < 0.01$) for the 6-, 8-, and 10-in. water cylinders and for the foot with 1.5- and 3-in. water background. The increase in tracking error due to cross-scatter was greater for larger objects.

4 Discussion

Biplane fluoroscopy is currently being used for motion analysis of various joints. This study measured the magnitude and effects of cross-scatter for a biplane fluoroscopic motion analysis system across a range of objects and kVp settings.

Figures 4 and 7 demonstrate the asymmetrical distribution of the detected cross-scatter signal, which was also demonstrated in previous studies of dual-source CT.[11–13] The asymmetrical distribution occurs because detected cross-scatter primarily originates from the rays that illuminate the surface of the object, and these rays are closer to one edge of the secondary detector (Fig. 4).[11–13]

The cadaver specimen experiments resulted in similar cross-scatter trends as for the water cylinders (Figs. 5 and 9). More specifically, the foot specimen CSF and tracking results were similar to the 4-in. water cylinder, the results for the foot +1.5-in. water background object were bounded by the 6- and 8-in. diameter cylinder results, and the results for the foot+3-in. water background object were bounded by the 8- and 10-in. diameter cylinder results. The similarity between the water cylinder and cadaver specimen results can be explained by the observation that the detected cross-scatter depends on the object surface, not the inhomogeneity within the object.[11,13]

The results demonstrated that CSF increased with phantom size and decreased with kVp, which matched the trends observed in previous dual-source CT studies.[12] Cross-scatter caused a greater reduction in CNR as the phantom size increased. The primary signal decreases with increasing object size, while the cross-scatter signal remains fairly constant with object size, leading to the overall increase in CSF with object size.[12] For the smaller phantoms (4 and 6 in.), the CSF was unaffected by gantry angle. For the larger phantoms (8 and 10 in.), the CSF increased with gantry angle. One possible explanation of this result is that at larger gantry angles, the detected cross-scatter photons originate from locations on the object surface that are closer to the cross-detector. The results of the simulation study suggest that a gantry angle of 60 deg may be advantageous for larger objects, although these results should be verified experimentally for the particular joint of interest.

The CSF values reported in Figs. 5, 6, and 8 were measured in ROIs in the center of the FOV. Cross-scatter increases toward the edge of the detector that is closest to the cross-beam, as shown in Fig. 4. However, for the cylindrical phantoms used in this study, the primary signal was lowest at the center of the FOV. Therefore, the CSF values estimated in this study generally represent the maximum CSF in the image and also the CSF at the location where the joints of interest would ideally be located.

Cross-scatter contamination did not significantly increase the tracking error in the 4-in. phantom or the cadaver foot specimen. Cross-scatter significantly increased the tracking error by 15%, 25%, and 38% for the 6-, 8-, and 10-in. phantoms, respectively, and increased error by 22% to 24% for the foot specimen with

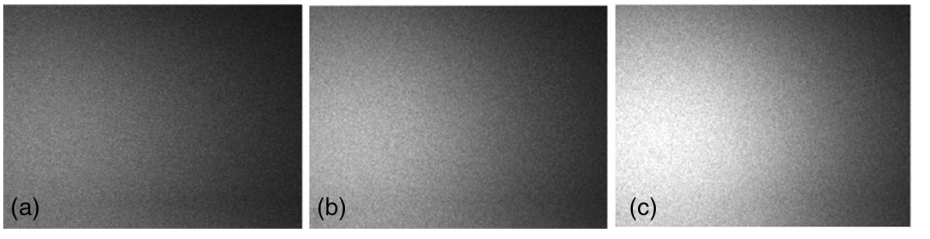

Fig. 7 Simulated cross-scatter images for the 10-in. phantom at 100 kV and at gantry angles of (a) 60 deg, (b) 75 deg, and (c) 90 deg. All images are windowed to display values from zero (black) to the highest value in the 90-deg image (white).

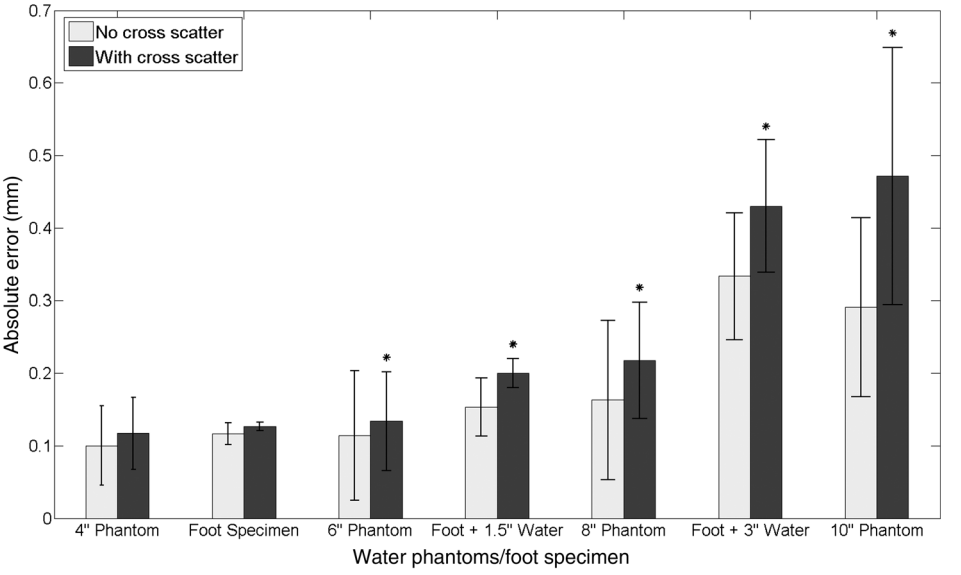

Fig. 9 Static tracking error for trials with and without cross-scatter as measured in the water phantoms and the foot specimen. Note: * signifies statistical significance ($P < 0.01$).

added water background. The tube current values (Table 1) were not optimized for each object size; therefore, the absolute error values presented in Fig. 9 could potentially be reduced by technique optimization. The purpose of this study was to quantify the relative effects of cross-scatter on motion accuracy, which are evident in Fig. 9. In the current study, the highest tracking error of 0.6 mm (± 0.5) for the 10-in. phantom with cross-scatter is smaller than the estimated 2.7- to 14.9-mm error due to skin movement artifacts of skin-mounted markers.[21]

The results suggest that marker-based tracking is possible on the submillimeter level for a range of phantom sizes and a cadaver foot specimen, even in the presence of cross-scatter contamination. The reduction in CNR due to cross-scatter may affect the accuracy of model-based tracking techniques. Model-based tracking methods optimize the bone positions and orientations by comparing projections of a 3-D bone model, generated from CT or MR data, to the fluoroscopic images.[10,14] The reduced CNR due to cross-scatter may decrease the accuracy of this 2-D to 3-D registration algorithm. An area of future work is to quantify the effects of cross-scatter contamination on the accuracy of model-based tracking in biplane systems.

This study did not consider the effects of varying the distance between the object and the detector. As in conventional x-ray imaging, a larger air gap is expected to reduce scatter. In motion-tracking biplane fluoroscopy systems, the object is generally placed as close to the detectors as possible in order to maximize the FOV. Therefore, larger air gaps are unlikely to be utilized for scatter rejection.

The biplane fluoroscopy system used in this study was designed for tracking the foot/ankle. Therefore, the walkway and force plate are in the beam path, as can be seen in Fig. 1. These objects contribute to the cross-scatter, although the results from the 4-in. phantom and the simulation results suggest that this contribution is small.

The objects investigated in this study were completely contained in the beam in the trans-axial direction. Therefore, the results are applicable to the tracking of extremities and joints that require complete object illumination, such as joints located near the object periphery. The results of this study may not be applicable to the imaging of interior regions of interest, such as the spine or biplane systems for interventional cardiology. When imaging interior regions of interest, proper beam collimation may reduce the illumination of the object surface near the cross-detector, which is expected to greatly reduce cross-scatter effects. However, tight collimation may be challenging for the imaging of moving joints. Previous work in dual-source CT demonstrated that beam-shaping filters decrease the CSF by reducing the fluence of the peripheral beam, which could potentially be applied to biplane fluoroscopy motion tracking.[13]

The significant increase in tracking error due to cross-scatter suggests that biplane fluoroscopy systems may benefit from the development of scatter rejection techniques for high-speed motion-tracking applications. Synchronous acquisition is currently required for motion estimation algorithms. Therefore, it may be beneficial to investigate grid mechanisms and beam-shaping filters that enable accurate motion tracking at high frame rates.

5 Conclusion

The results demonstrated negligible cross-scatter effects for biplane fluoroscopy imaging of the 4-in. phantom and the foot cadaver specimen, suggesting negligible motion-tracking error due to cross-scatter for distal extremities. The cross-scatter fraction ranged from 0.4 to 0.9 for the 6-in. through 10-in. phantoms, with CNR decreasing by 15% to 36%. Cross-scatter significantly increased the marker tracking error for the 6-, 8-, and 10-in. phantoms and for the foot specimen with added water background. These results suggest that the accuracy of motion analysis of larger anatomical regions, such as the shoulder or spine, may be degraded due to cross-scatter. Submillimeter tracking accuracy was attained in this study for all phantoms, despite increasing cross-scatter effects with phantom size.

Acknowledgments

The contents of this paper were developed under a grant from the Department of Education, NIDRR Grant No. H133E100007. However, those contents do not necessarily represent the policy

of the Department of Education, and you should not assume endorsement by the federal government. We would also like to thank Jessica Fritz and Chuck Wilson for their assistance in the laboratory during data collection.

References

1. M. J. Bey et al., "Validation of a new model-based tracking technique for measuring three-dimensional, in vivo glenohumeral joint kinematics," *J. Biomech. Eng.* **128**(4), 604–609 (2006).
2. W. J. Anderst et al., "Validation of a noninvasive technique to precisely measure in vivo three-dimensional cervical spine movement," *Spine* **36**(6), E393–E400 (2011).
3. Q. Xia et al., "In-vivo motion characteristics of lumbar vertebrae in sagittal and transverse planes," *J. Biomech.* **43**, 1905–1909 (2010).
4. W. J. Anderst et al., "Validation of three-dimensional model-based tibiofemoral tracking during running," *Med. Eng. Phys.* **31**(1), 10–16 (2009).
5. M. J. Bey et al., "Accuracy of biplane x-ray imaging combined with model-based tracking for measuring in-vivo patellofemoral joint motion," *J. Ortho. Surg. Res.* **3**, 38 (2008).
6. A. Cappozzo et al., "Position and orientation in space of bones during movement: experimental artefacts," *Clin. Biomech.* **11**(2), 90–100 (1996).
7. C. Nester et al., "Foot kinematics during walking measured using bone and surface mounted markers," *J. Biomech.* **40**, 3412–3423 (2007).
8. B. A. Maslen and T. R. Ackland, "Radiographic study of skin displacement errors in the foot and ankle during standing," *Clin. Biomech.* **9**(5), 291–296 (1994).
9. E. L. Brainerd et al., "X-ray reconstruction of moving morphology (XROMM): precision, accuracy and applications in comparative biomechanics research," *J. Exp. Zool.* **313A**(5), 262–279 (2010).
10. D. L. Miranda et al., "Static and dynamic error of a biplanar videoradiography system using marker-based and markerless tracking techniques," *J. Biomech. Eng.* **133**(12), 121002 (2011).
11. K. J. Engel, C. Herrmann, and G. Zeitler, "X-ray scattering in single-and dual-source CT," *Med. Phys.* **35**(1), 318–332 (2008).
12. W. Giles et al., "Interleaved acquisition for cross scatter avoidance in dual cone-beam CT," *Med. Phys.* **39**(12), 7719–7728 (2012).
13. Y. Kyriakou and W. A. Kalender, "Intensity distribution and impact of scatter for dual-source CT," *Phys. Med. Biol.* **52**(23), 6969 (2007).
14. B. M. You et al., "In vivo measurement of 3-D skeletal kinematics from sequences of biplane radiographs: application to knee kinematics," *IEEE Trans. Med. Imaging* **20**(6), 514–525 (2001).
15. S. Agostinelli et al., "Geant4: a simulation toolkit," *Nucl. Instrum. Methods A* **506**(3), 250–303 (2003).
16. K. Cranley et al., "Catalogue of diagnostic x-ray spectra and other data," IPEM Report No. 78 (1997).
17. T. L. Hedrick, "Software techniques for two- and three- dimensional kinematic measurements of biological and biomimetric systems," *Bioinsp. Biomim.* **3**, 034001 (2008).
18. L. Chen, C. W. Armstrong, and D. D. Raftopoulos, "An investigation on the accuracy of three-dimensional space reconstruction using the direct linear transformation technique," *J. Biomech.* **27**(4), 493–500 (1994).
19. J. P. Fillard, "Sub-pixel accuracy location estimation from digital signals," *Opt. Eng.* **31**(11), 2465–2471 (1992).
20. B. F. Alexander and K. C. Ng, "Elimination of systematic error in subpixel accuracy centroid estimation," *Opt. Eng.* **30**(9), 1320–1331 (1991).
21. R. Shultz, A. E. Kedgley, and T. R. Jenkyn, "Quantifying skin motion artifact error of the hindfoot and forefoot marker clusters with the optical tracking of a multi-segment foot model using single-plane fluoroscopy," *Gait Posture* **34**(1), 44–48 (2011).

Janelle A. Cross is an assistant professor in the Department of Orthopedic Surgery at the Medical College of Wisconsin and the director of the Sports Medicine Research Division. She received her PhD in biomedical engineering from Marquette University in 2015. Her research interests include sport biomechanics, injury mechanisms, and rehabilitation engineering.

Ben McHenry received his BS degree in mechanical engineering in 2002 from the Milwaukee School of Engineering, Milwaukee, Wisconsin, and his PhD in biomedical engineering in 2013 from Marquette University, Milwaukee, Wisconsin. Currently, he is a postdoctoral fellow in biomedical engineering at Marquette University.

Taly Gilat Schmidt is an associate professor of biomedical engineering at Marquette University, where she directs the Medical Imaging Systems Laboratory. Her research interests include medical imaging system design, optimization, and reconstruction. She received her PhD in electrical engineering from Stanford University.